

Electronic confinement of surface states in a topological insulator nanowire

Ruchi Saxena,¹ Eytan Grosfeld,² Sebastian E de Graaf,³ Tobias Lindstrom,³ Floriana Lombardi,⁴ Oindrila Deb,¹ and Eran Ginossar¹

¹*Advanced Technology Institute and Department of Physics, University of Surrey, Guildford, GU2 7XH, United Kingdom*

²*Department of Physics, Ben-Gurion University of the Negev, Beer-Sheva 8410501, Israel*

³*National Physical Laboratory, Hampton Road, TW11 0LW, Teddington, United Kingdom*

⁴*Quantum Device Physics, Chalmers University of Technology, Sweden*

(Dated: June 29, 2022)

We analyze the confinement of electronic surface states in a model of a topological insulator nanowire. Spin-momentum locking in the surface states reduces unwanted backscattering in the presence of non-magnetic disorder and is known to counteract localization for certain values of magnetic flux threading the wire. We show that intentional backscattering can be induced for a range of conditions in the presence of a nanowire constriction. We propose a geometry for a nanowire that involves two constrictions and show that these regions form effective barriers that allow for the formation of a quantum dot. We analyze the zero-temperature non-interacting electronic transport through the device using the Landauer-Büttiker approach and show how externally applied magnetic flux parallel to the nanowire and electrostatic gates can be used to control the spectrum of the quantum dot and the electronic transport through the surface states of the model device.

I. INTRODUCTION

Topological insulators (TI) are bulk insulators that exhibit surface states with unique electronic properties. Three-dimensional (3D) TI nanowires (TINWs) are promising candidates for studying the electronic surface transport¹⁻⁴; they admit two-dimensional (2D) helical surface states that prohibit backscattering and reduce localisation in the absence of magnetic disorder while reducing any residual bulk transport due to their geometry⁵⁻⁹. While this protection from unintended scattering harbours promise, designing mesoscopic scale structures that can exploit the topological protection does require control of the electronic transport, including methods to control transmission and to generate electronic confinement (e.g., quantum dots, quantum point contacts). Successful control of charge transport would pave the way for various applications of TIs ranging from improved spintronic devices, through more accurate charge pumps for quantum metrology to quantum computing¹⁰⁻¹³.

There have been various theoretical proposals for inducing a gap in the surface spectrum of the TIs since this would allow to achieve the electronic confinement and control needed for practical devices. These include exploiting the exchange coupling induced by a proximitised magnetic insulator¹⁴, by means of surface pairing through a proximitised superconductor¹⁵, or realising a tunnel coupling between the top and bottom surfaces of an ultra-thin TI¹⁶⁻¹⁹. The latter method has been experimentally explored in a quantum dot fabricated from a thin film of a 3D TI with a gate tunable barrier. It was found by varying the gate voltage that the charge transport ranged from ohmic to tunneling regimes²⁰, although signatures of quantised levels localised within the dot region remained elusive. On the other hand, geometrically constructed quantum devices for charge

confinement have not been fully explored in TINWs.

TINWs are promising with regards to realising full electronic confinement, and progress in understanding transport was made in recent works which studied effects of disorder, ripples and magnetic fields²¹⁻²⁴. Recently, signatures of the sub-bands of the TI nanowire have been detected experimentally²⁵ creating additional motivation to analyse the potential of such devices for quantum confinement along the nanowire.

In this work we show, by analysing the conditions for quantum confinement within a defined section of a long TINW, that a quantum dot can be created which transport is uniquely based on the nature of the topological surface states. The emergence of the quantum dot in our work is strictly a quantum mechanical effect which is based on the quantum interference of the Dirac surface states. The analysis is based on an effective cylindrical model for a microstructure with defined radius variations and external electric and magnetic potentials. A key element is a reduced radius region (constriction) exhibiting an increased gap in the spectrum of surface states. We show that this region acts like a potential barrier which can backscatter Dirac electrons²². Conditions for charge confinement can be found when backscattering in the TINW is allowed between non-time reversal symmetric states as well as for cases where backscattering is facilitated by the dynamics in the constrictions where time-reversal symmetry (TRS) is broken. The radius variation is essential when the TINW is flux-biased to the gapless state of half-flux for which the surface states are topologically protected from backscattering by scalar potentials. This is considered to be the point of optimal performance due to the resilience against disorder in the leads. Based on this, we propose a geometrical construction that can lead to resonant tunnelling²⁶ and form discrete states within a confined central region, see Fig. 1. We show

that the geometry exhibits clear evidence of quantum dot formation that is manifested in the electronic transport as sub-gap resonances.

The remainder of this paper is organised as follows. In section II, we present the geometrical construction of a TINW for a quantum dot and discuss the scattering between incoming and reflected states that can lead to finite reflection. In section III, we describe the Hamiltonian and the scattering matrix for the model device to compute the conductance employing the Landauer-Büttiker approach. We also investigate the effect of the curved interface on the motion of the surface states by incorporating the spin connection which is essential to analyze the motion of Dirac particle on a curved space time^{21,27-29}. We discuss the numerical results in section IV and conclude our findings in section V.

II. PROPOSED GEOMETRY

We start by presenting the proposed geometry for the TINW quantum dot (Fig. 1a). We consider a cylindrical nanowire of radius R_1 , which is etched at two regions to a radius R_2 ($R_2 < R_1$). We label this device NCNC where “N” refers to the region with radius R_1 and “C” denotes the region with the reduced radius R_2 . Both regions are assumed to have full rotational-symmetry around the wire axis. The wave functions in each region satisfy an anti-periodic boundary condition around the nanowire perimeter due to the curvature-induced π Berry phase. As detailed in section III, due to the radius dependent band gap in the TINW^{30,31}, the band-gap profile experienced by the incoming electronic states is expected to behave as shown schematically in Fig. 1b. Etching is expected to have some gradual radius profile, as depicted in Fig. 1c. To incorporate its effect on the electronic transport we model the interface using a z -dependent radius, as demonstrated in Fig. 1d, with

$$R(z) = R_1 + (R_2 - R_1)F(z), \quad (1)$$

where $F(z) = \frac{1}{2} \left[1 + \frac{2}{\pi} \tan^{-1} \left(\frac{z}{a} \right) \right]$ is the smooth Heaviside theta function with the parameter a tuning the interface from step-like (small a) to smooth (large a).

Controlled reflection of the electrons from the interfaces is essential to realising charge confinement. The motion of the particle belonging to a specific sub-band can be thought of as one-dimensional (only dispersing along the wire axis) with the gap proportional to the angular momentum l . The incoming and reflected states of same l are not Kramers pairs and hence, are prone to backscattering due to disorder^{22,30,32}. The unusual finite reflection here is strikingly different than the zero reflection (unit transmission) situation where backscattering is prohibited due to the spin-momentum locked gapless and orthogonal surface states. The scattering between non-orthogonal surface states in TINW, characterised by k of opposite sign and same l , can be thought to be a result of the finite angular momentum. Similar scattering

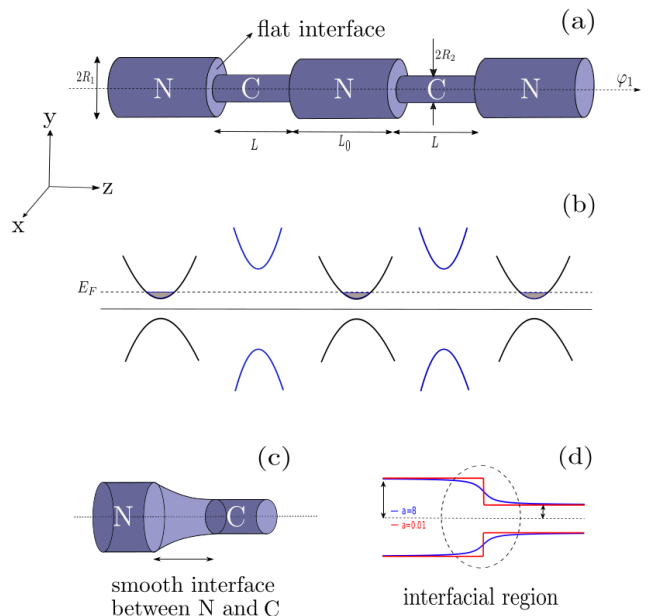


Figure 1. Geometrical model of the quantum dot based on a 3D TINW: (a) The geometry used for the theoretical study of the transport properties. N and C denote regions of radius R_1 and the reduced radius regions of radius R_2 formed by etching the wire respectively. The interfaces between N and C regions are drawn flat for simplicity. (b) The bandgap profile (as explained in the main text) experienced by an incident electron. (c) A smooth interface connecting the N and C regions of the TINW. (d) The radius dependence of the TINW as function of the coordinate z along the wire with the parameter $a = 8$ corresponding to (c) and $a = 0.01$ generating a step-like interface.

is paradigmatic to the suppression of Klein tunnelling in graphene^{33,34} and in TIs^{35,36} when a massless Dirac fermion is incident at an oblique angle to the potential barrier. A finite transverse component of the momentum arising from the oblique incidence allows backscattering of the incident Dirac fermions³⁶⁻⁴⁰ due to the non-orthogonal incoming and reflected states.

III. SURFACE HAMILTONIAN AND SCATTERING ANALYSIS

The Hamiltonian for the surface states of a non-uniform 3D TINW can be derived using a field theoretic approach²¹⁻²⁴. We provide the derivation of the Hamiltonian in the Appendix for notational convenience. To include the coaxial magnetic field we use the symmetric gauge to write the vector potential $A_\phi = -Br/2 = -\Phi/2\pi r$, where ϕ denotes the azimuthal direction, r is the radial coordinate, and Φ is the magnetic flux along the nanowire axis. With the minimal coupling of the magnetic field to the transverse motion of the Dirac sur-

face states the Hamiltonian becomes

$$H = \hbar v_F \left[\frac{1}{\sqrt{1 + R'(z)^2}} \left\{ i\partial_z + \frac{iR'(z)}{2R(z)} \right\} \sigma_y + \frac{1}{R(z)} (-i\partial_\phi - \varphi) \sigma_z \right], \quad (2)$$

where $R(z)$ is the radial function which is defined to model the interface between N and C regions and $\varphi = \Phi/\Phi_0$ is the dimensionless magnetic flux. The term proportional to R' is the spin-connection contribution to the Dirac fermions moving along the curved surface^{21–24}. This Hamiltonian is particularly useful for finding the appropriate boundary condition at the curved interface between the normal and reduced radius regions. We note that we only consider the orbital effect of the applied magnetic field because at low magnetic field (e.g. $\varphi = 0.5$), the Zeeman energy is negligible compared to the energy spacing of the sub-bands⁴¹.

For the cylindrical surfaces in the N and C regions, away from the interface, $R' = 0$. For this case, exploiting the rotational symmetry of the cylinder and translational invariance along the wire axis we can write the solution of the time-independent Schrödinger equation for this Hamiltonian as

$$\Psi_{k,l}(z, \phi) = e^{ikz} e^{il\phi} \psi_{k,l}, \quad (3)$$

here ψ is a two component spinor and l is a half-integer angular momentum due to the presence of a π spin Berry phase acquired by the 2π rotation of the spin around the cylindrical surface^{4,27,42}. Using the solution given in Eq.3 the Hamiltonian in N and C regions can be written as

$$H_{1,2} = \hbar v_F \left[-k\sigma_y + \left(\frac{l - \varphi_{1,2}}{R_{1,2}} \right) \sigma_z \right]. \quad (4)$$

The energy of the surface states can be found by diagonalizing the above Hamiltonian,

$$E_{1,2} = \pm \hbar v_F \sqrt{k_{1,2}^2 + (l - \varphi_{1,2})^2 / R_{1,2}^2},$$

where 1,2 refers to N and C region respectively. Due to the reduced cross section in the C region, the flux penetrating into this region is given by $\varphi_2 = \varphi_1 R_2^2 / R_1^2$.

We now explain the scattering processes in Fig. 2 where we schematically show the allowed and forbidden scattering between the right and left moving spinors. Note that the magnetic flux threaded along the wire axis breaks TRS and all the surface states become non-degenerate. However, TRS can be restored at integer and half-integer values of magnetic flux and all bands, except the $l = \varphi$ band become degenerate^{23,27,30,43}. Now, if we fix the Fermi energy within the bulk gap such that it crosses

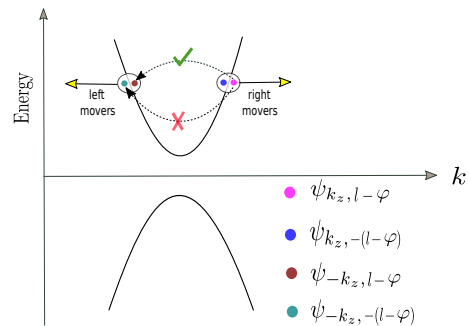


Figure 2. The allowed and forbidden scattering between orthogonal ($\psi_{k_z, l-\varphi}$ (pink colour) and $\psi_{-k_z, -(l-\varphi)}$ (green colour)) and non-orthogonal states ($\psi_{k_z, l-\varphi}$ (pink colour) and $\psi_{-k_z, l-\varphi}$ (brown colour)) is shown schematically.

the lowest degenerate sub-band (which happens at integer values of magnetic flux), there always exists two right moving spinors $\psi_{k_1, \pm(l-\varphi)}$ and two left moving spinors $\psi_{-k_1, \pm(l-\varphi)}$ as demonstrated in Fig. 2. As discussed in section 1, although the backscattering is prohibited between the time-reversal partner $\psi_{k_1, l-\varphi}$ and $\psi_{-k_1, -(l-\varphi)}$, it is allowed between two other available non-orthogonal states $\psi_{k_1, l-\varphi}$ and $\psi_{-k_1, l-\varphi}$. As a result, the non-magnetic disorder can backscatter the Dirac surface states.

First, we analyse a uniform nanowire for the case of zero magnetic flux. We consider the scattering of surface states belonging to the $l = 1/2$ band in presence of a double barrier electrostatic potential V induced by gates in a TINW with uniform radius, see Fig. 3a. Notice that due to a non-zero potential, there is a uniform upward shift in the energy spectrum as shown in Fig. 3b which creates a finite energy difference between the conduction bands belonging to the section with potential V and the section without the potential. By fixing the energy of the incoming surface state within this energy window, we compute the transmission through the TINW for zero magnetic flux and find sub-gap (the gap between the conduction band for $V=10$ meV and $V=0$ in Fig. 3b) resonances in the transmission probability function of the surface states through the TINW as shown in Fig. 3c, which is a typical signature of bound state formation within the middle region. The formation of bound states indicate the fact that surface states in a TINW can backscatter from a scalar disorder (non-magnetic disorder).

For a half-integer value of flux along the nanowire, there is always a corresponding value of l for which the surface state is non-degenerate and gapless^{23,30}. In this particular state, an electrostatic barrier as shown in Fig. 3a, can not backscatter the Dirac particles. Thus, in order to generate confinement we need an additional mechanism to ensure a finite gap in the constrictions in the TINW system. Hence, we propose to have reduced ra-

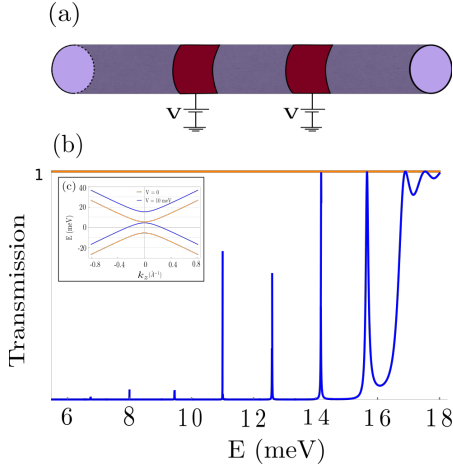


Figure 3. (a) The uniform TINW in presence of two electrostatic potentials V . (b) If the energy of the incoming state is fixed between the conduction band for $V=10$ meV and $V=0$ sub-gap transmission resonances are found within the region between the potential barrier. The inset shows the dispersion of the $l = 1/2$ band in a uniform nanowire of radius 30 nm for zero flux in the absence (orange colour) and presence (blue colour) of a potential barrier.

dius regions in the TINW so that the flux penetrating these regions is not a half-integer as opposed to N region. Consequentially, the surface states at these constricted regions become gapped due to the breaking of TRS. To summarize, constricted region ensures a larger band gap between the surface states as compared to N region for both with and without magnetic flux.

The external flux control on the electronic transport through the clean NCNCN geometry is a unique feature of the TINW quantum dot where each C region has radius $R_2 < R_1$. The finite reflection due to breaking of TRS in C regions resembles the backscattering in quantum spin Hall edge in the presence of local magnetic disorder that breaks the TRS³⁵. Furthermore, the external gate tunability of the band gap in the constricted region can provide another probe to control the electronic transport through the model device. In section IV, we discuss both external magnetic flux and gate dependent transport in detail.

Now, we present the scattering matrix approach to find the scattering coefficients for the non-interacting electrons. Let us consider the interface at $z = 0$ between an N and a C region in the presence of a finite flux along the nanowire axis. We compute the transfer matrix that connects the wave function from the left side of the interface ($\psi(z < 0)$) to the right side of it ($\psi(z > 0)$). This can be done by solving the Schrödinger equation $H\psi = E\psi$, where H is given by Eq.(4). By integrating the Schrödinger equation across the interface we arrive at the following wave function matching condition (for

the curved interface as shown in Fig.1c)

$$\psi(z > 0) = T_z \psi(z < 0), \quad (5)$$

where the 2×2 transfer matrix T_z is given by

$$T_z = \mathcal{P}_z \text{Exp} \left[\int_{z_0}^{z_1} \left\{ \frac{-R'}{2R} - \frac{\sqrt{1+R'^2}}{R} (l - \varphi) \sigma_x - \frac{iE\sqrt{1+R'^2}}{\hbar v} \sigma_y \right\} dz \right], \quad (6)$$

here \mathcal{P}_z is the path ordered product of the exponential factor along the wire.

Next, considering the elastic scattering within the device we can write the wave functions in each region of the model device shown in Fig.1a as

$$\begin{aligned} \psi_{1,3,5} &= \frac{a_{1,3,5}}{\sqrt{2}} \begin{pmatrix} \frac{-\chi_l + E}{ik_1} \\ 1 \end{pmatrix} e^{ik_1 z} + \frac{b_{1,3,5}}{\sqrt{2}} \begin{pmatrix} \frac{-\chi_l + E}{-ik_1} \\ 1 \end{pmatrix} e^{-ik_1 z} \\ \psi_{2,4} &= a_{2,4} \begin{pmatrix} \frac{-\chi_2 + E}{ik_2} \\ 1 \end{pmatrix} e^{ik_2 z} + b_{2,4} \begin{pmatrix} \frac{-\chi_2 + E}{-ik_2} \\ 1 \end{pmatrix} e^{-ik_2 z}, \end{aligned} \quad (7)$$

here $\psi_{1,3,5}$ and $\psi_{2,4}$ are the wave functions in the normal N and reduced radius regions C respectively and $k_{1,2} = \sqrt{E^2 - \chi_{1,2}^2}$, $\chi_{1,2} = (l - \varphi_{1,2})/R_{1,2}$. $a_{1,2,3,4,5}$ and $b_{1,2,3,4,5}$ are the scattering coefficients. Here 1,3,5 refers to N regions while 2,4 indicates C regions. We use the wave function matching condition given in Eq.(5) to find the total transfer matrix M that connects the incoming states in the leftmost N region to the outgoing states in the right most N region and we get

$$M = \alpha_1^{-1} T_z \beta_1 \alpha_2^{-1} T_z^\dagger \beta_2 \alpha_3^{-1} T_z \beta_3 \alpha_4^{-1} T_z^\dagger \beta_4, \quad (8)$$

where $\alpha_{1,2,3,4}$ and $\beta_{1,2,3,4}$ are given as

$$\begin{aligned} \alpha_i &= \begin{pmatrix} \frac{-\chi_i + E}{ik_i} e^{ik_i z_i} & \frac{-\chi_i + E}{-ik_i} e^{-ik_i z_i} \\ e^{ik_i z_i} & e^{-ik_i z_i} \end{pmatrix} \\ \beta_i &= \begin{pmatrix} \frac{-\chi_i + E}{\sqrt{2}ik_i} e^{ik_i z_i} & \frac{-\chi_i + E}{-\sqrt{2}ik_i} e^{-ik_i z_i} \\ e^{ik_i z_i} & e^{-ik_i z_i} \end{pmatrix} \\ \alpha_3 &= \alpha_1 \quad (\text{at } z_1 = z_3) \\ \alpha_4 &= \alpha_2 \quad (\text{at } z_2 = z_4) \\ \beta_3 &= \beta_1 \quad (\text{at } z_1 = z_3) \\ \beta_4 &= \beta_2 \quad (\text{at } z_2 = z_4), \end{aligned} \quad (9)$$

Here $i = 1, 2, 3, 4, 5$ as before. The inverse of the matrix element M_{11} gives the transmission probability which we use in the next section to discuss the characteristics of the quantum dot device proposed in this work.

IV. NUMERICAL RESULTS

We now discuss the zero-temperature electronic transport through the nanowire structure. We consider the

energy of the incoming states such that they are propagating modes in N regions (with radius R_1) and the radius of C regions is always smaller than R_1 . The propagating states with total angular momentum $l = 1/2$ coming from the left side of the device can have a finite reflection at the first interface between N and R. This is due to non-orthogonality of the incoming state $\psi_{k_1, (l-\varphi)}$ and the outgoing states $\psi_{-k_1, (l-\varphi)}$ which are not the time reversal partner. Since the C regions have larger gap than in N, these constricted regions effectively behave like the potential barrier for the Dirac particles and thus can scatter the incoming particles. The multiple scattering events in the middle region of NCNCN give rise to resonance effects which manifest in the total transmission function through the device. We employ the Landauer-Büttiker approach⁴⁴ to compute the conductance through the NCNCN device at zero temperature and plot it in Fig.4a (red colour) as a function of the chemical potential μ for the flat interface which corresponds to the boundary condition with $T_z = 1$. In experiments, μ is influenced by substrate, contacts etc. and can be locally tuned using electrostatic gates. The conductance peaks correspond to the sub-gap resonances in the transmission probability through the model device and exhibit clear evidence of bound states formation inside the middle N region of the device. Notice that the N regions are immune to scalar disorder for $\varphi = l$ due to appearance of gapless surface states. More generally, when the dimensions of the middle section is small compared to the mean free path, we do not expect disorder to significantly affect the resonances.

The position of the conductance peaks in Fig.4a gives the energy of the bound states. The width of a conductance peak depends on the length L of the C regions while the number of these peaks depends on the length L_0 of the middle N region (the confined region) where we find the bound states. The value of the model parameters used in this work are chosen as $R_1 = 80$ nm, $R_2 = 15$ nm, $L = 80$ nm, $L_0 = 100$ nm and $\varphi_1 = 0.5$ which are experimentally attainable^{1,2,25}. Surface sensitive experiments on Bi_2Se_3 estimate the value of the coherence length to be 500 nm and a typical value of the mean free path to be 100 nm^{1,25,41}. Therefore, the electronic transport in the TINR studied in this work is expected to be ballistic and phase coherent. It is important to note that device parameters can be found for the case with one non-degenerate sub-gap resonance. In that case, only one electron can be inside the dot. However, there will be multiple quantum dot states for a larger quantum dot. We show the transmission through the device for a larger dot of length $L_0 = 400$ nm and same radius $R_2 = 15$ nm in Fig. 4b which exhibits many sub-gap resonances in the transmission function. A useful quantity in the discussion of quantum dot is the charging energy $E_c = e^2/C_0$, where C_0 is the capacitance that depends on the device dimensions and the dielectric constant of the material. The value of C_0 can be inferred

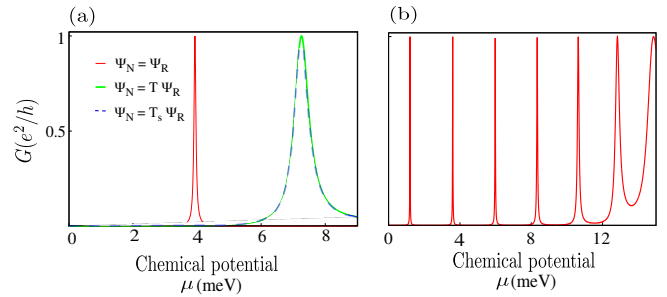


Figure 4. (a) Conductance through an etched TI nanowire with flat interfaces (as sketched in Fig.(1a)) is plotted as a function of chemical potential μ for a dot length $L_0 = 100$ nm. Red colour depicts the result for flat interface. The position of conductance peaks not only shifts but also broadens in case of curved interface as shown by the blue (dotted) and green (solid) curves (here, former and later colour represent the result with and without incorporating spin connection for the curved manifold). It is due to the modified boundary conditions (see, Eq.(6)). More detail about the boundary conditions in all three cases is discussed in the main text. (b) Sub-gap resonant transmission through the long quantum dot $L_0 = 400$ nm in TI nanowire NCNCN geometry having flat interfaces. The numerical values of the system parameters are chosen as $R_1 = 80$ nm, $R_2 = 15$ nm, $L = 80$ nm, $\varphi_1 = 0.5$ and $\varphi_2 = \varphi_1 R_2^2/R_1^2$.

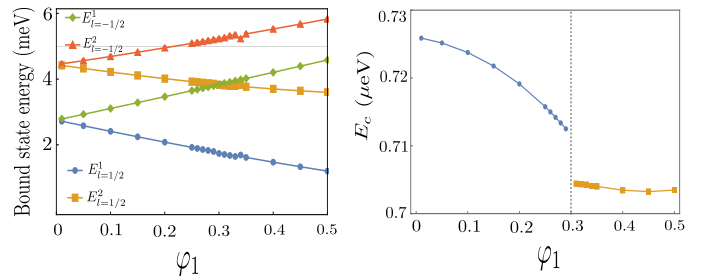


Figure 5. (a) The lowest two bound state energies as a function of the magnetic flux φ_1 for $l = 1/2$ and $l = -1/2$. (b) Quantum contribution to the Coulomb energy (E_c^q) as a function of the magnetic flux. The dotted line in (b) is drawn to represent the degeneracy point. Other parameters are the same as in Fig.4b.

from the experiments based on Bi_2Se_3 nanowires. For a Bi_2Se_3 nanowire on a SiO_2/Si substrate $C_0 = 2 \times 10^{-17}$ F for a surface area 8.6×10^{-14} m² was found²⁰, giving an effective capacitance $C_{\text{eff}} = 2.3 \times 10^{-4}$ F m⁻². We can now estimate the charging energy of the quantum dot ($R_2 = 15$ nm, $L_0=400$ nm) using²¹, $E_c = e^2/2\pi R_1 L_0 C_{\text{eff}}$ and this gives 3.6 meV. I.e. Coulomb blockade like oscillations of the conductance are expected in transport experiments on a large dot by varying the gate voltage applied to the central NCNCN region. However, as we pointed out earlier, the origin of the discrete quantum dot states here uniquely arises from interference of the

surface states, different from the appearance of quantum dot based on Coulomb blockade.^{45,46}

Next, we examine the effect of a curved interface. We utilize the radial function given in Eq.(1) of the section II to incorporate the curvature effects on the electronic transport. Here, we use the boundary condition, $\psi(z > 0) = T_z \psi(z < 0)$ where T_z is the transfer matrix for $R' = 0$. It is clear from Fig.4a (blue curve) that not only the position of the conductance peak gets shifted but also the peak broadens compared to the situation when we consider the flat interface. Furthermore, we analyse the motion of the Dirac particle on the curved interface incorporating the spin connection in the transfer matrix ($R' \neq 0$). We plot the conductance again in Fig. 4a (green curve) which coincides with the plot computed for $R' = 0$ (blue colour). The findings suggest that the electronic transport is unaffected by the inclusion of the spin connection.

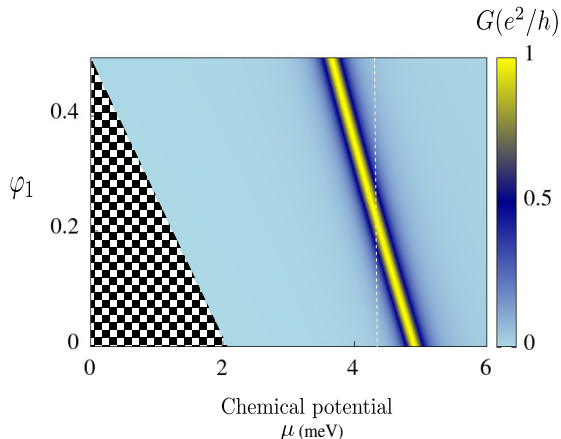


Figure 6. Conductance as a function of chemical potential μ and the flux along the wire axis φ_1 . Device parameters are fixed at $R_1 = 80$ nm, $R_2 = 20$ nm, $L = 80$ nm and $L_0 = 100$ nm. The checker board region is non-physical because of the evanescent modes in N region.

Apart from the classical charging energy of the formed quantum dot, which arises from the long range Coulomb potential, we also estimate the quantum contribution E_c^q due to the screened short-range Coulomb interaction⁴⁷ which depends on the quantum dot states. We study its dependence on the magnetic flux. In Fig.5a, we show how the energy of the bound states varies as a function of magnetic flux φ_1 . We represent the lowest two bound states corresponding to the $l = 1/2$ and $l = -1/2$ bands as $E_{l=1/2}^1$, $E_{l=1/2}^2$ and $E_{l=-1/2}^1$, $E_{l=-1/2}^2$ respectively in Fig.5a. We model the short-range interaction as a contact interaction and compute the Coulomb energy between electrons which occupy the two lowest energy states. For $\varphi_1 < 0.3$, the two occupied states correspond to $E_{l=1/2}^1$ and $E_{l=-1/2}^1$ while $E_{l=1/2}^2$ and $E_{l=-1/2}^2$

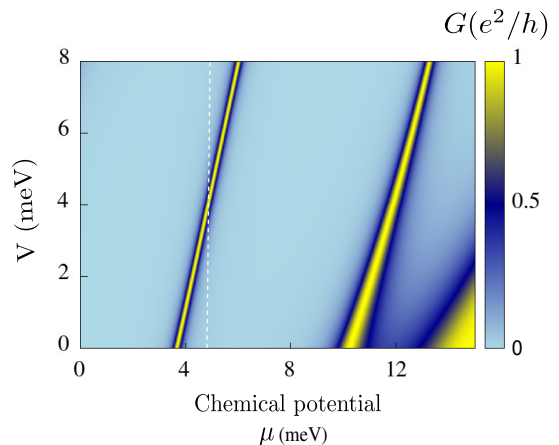


Figure 7. External gate tunability of the conductance is shown as a function of the electric potential induced on the dot by the electrostatic gates applied in the C regions and the chemical potential μ . The values of other parameters are taken as in Fig.6.

become the lowest energy states for $\varphi_1 > 0.3$. We plot the Coulomb energy E_c^q in Fig.5b as a function of flux φ_1 . We observe a smooth decay in E_c^q as the magnetic flux increases up until the point of degeneracy at $\varphi_1 = 0.3$. As flux increases beyond 0.3 we notice slow decrease in E_c^q . We note that we do not estimate E_c^q at one point $\varphi_1 = 0.3$ as the second lowest quantum dot state is degenerate, see Fig.5a.

The bandgap tunability of the surface state by an external flux enables us to investigate the electronic transport as a function of the flux threaded along the wire axis. We plot the conductance through the model device in Fig. 6 for the flat interfaces between the N and C regions as a function of chemical potential μ and the flux φ_1 applied along the wire axis in the N region. Evidently, if the chemical potential is fixed (consider the dotted white line in the plot) the transport of the surface states can be externally controlled by the application of a flux along the wire. The checker board region in Fig. 6 corresponds to the presence of evanescent modes in the N region and hence is non-physical. Next, we examine the gate voltage tunability of the electronic transport in presence of half-integer flux. The two gate voltages in C regions change the band gap profile by shifting the band spectrum (with respect to the band spectrum in N regions) upward by the electrostatic potential V applied by the gate. We plot the conductance as a function of induced gate potential and the chemical potential in Fig. 7 for flux $\varphi_1 = 0.5$ and we find that the conductance can be controlled by varying the gate voltage.

So far, we study the quantum dot considering the flat interfaces between different sections of the device. However, while etching/patterning nanowire the interfaces are likely to undergo geometrical deformation. As dis-

cussed earlier in section II, to address the transport in this situation, we model the interface as shown in Fig.1d and assume a smoothness $a = 8$ nm, a relatively smooth interface that is obtainable using modern nanofabrication techniques, yet significantly smaller than other dimensions of the NCNCN structure. We investigate the influence of such interfaces on the electronic transport as a function of external flux, gate voltages and chemical potential. First, we show the conductance as we vary flux and chemical potential in Fig.8. We observe that the resonance line broadens and gets shifted on the energy axis. The broadening of the conductance peak relates to the inverse of the life time of the quantum dot state which means that the particle would quickly escape the dot. Similar features are found when we plot conductance as a function of chemical potential and the gate voltage in Fig.9. These results can be attributed to the strong coupling of the dot to the left and right N regions which determines the shape and position of the conductance peaks. Thus, from an experimental point of view it is important to engineer as sharp interfaces as possible.

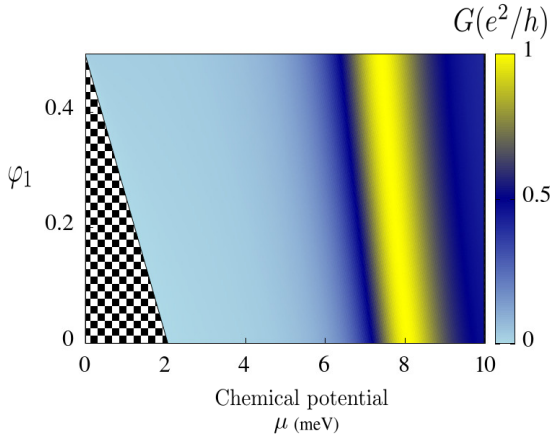


Figure 8. The conductance through the NCNCN quantum dot model considering the smooth interface (taking $a=8$ nm, as shown in Fig.1d) as a function of chemical potential and magnetic flux φ_1 . The values of all parameters are the same as in Fig.6.

The external control of quantum transport is a necessary prerequisite in the fabrication of field-effect transistors and other quantum devices. The external magnetic flux as well as induced gate voltage tunability makes our geometrical construction of the TI quantum dot experimentally feasible for experimental implementation. Moreover, we anticipate that the transmitted current through the quantum dot states in this device might have different spinor state for different conditions fixed by chemical potential, magnetic flux and voltage bias. We leave the thorough study of characterising the finite temperature current in presence of Coulomb interaction and disorder for degenerate and non-degenerate dot for future work.

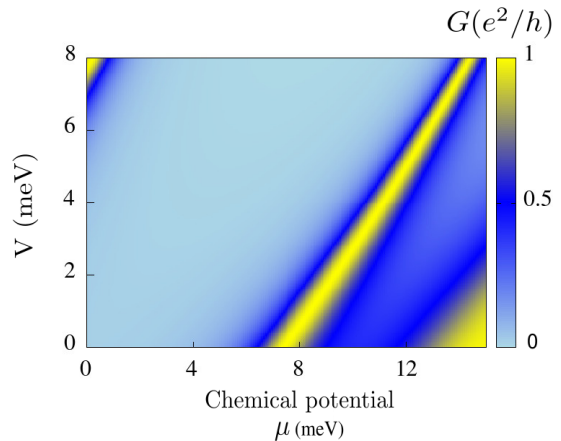


Figure 9. The conductance through the NCNCN quantum dot model considering the smooth interface (the same as for Fig.8) as a function of chemical potential and external gate voltage. The values of all parameters are the same as in Fig.6.

V. CONCLUSIONS

In this work, we exploited the finite reflection processes for designing a model for a quantum dot in a TINW. We showed that finite reflection is possible essentially due to the transverse angular momentum modes. We demonstrated that in the presence of double barrier potential, the uniform nanowire can host bound states if the Fermi energy lies within the conduction band minimum for $V \neq 0$ and $V = 0$ for a fixed value of angular momentum l . We elucidated the necessity of the constricted region in presence of half-integer magnetic flux along the wire axis in N region (half-integer magnetic flux is important to prevent the backscattering due to accident disorder in N region). In particular, we propose a theoretical model of a quantum dot in a TINW exploiting the unique characteristics of the surface states and show that the confining potential due to the larger gap in the surface states in constricted regions localise the Dirac surface state. Finally, we explicitly show that the electronic transport through discrete quantum dot states can be modulated by external magnetic flux and gate voltage. This will facilitate some of the most desirable quantum devices for metrology (single-electron devices, charge pumps), spintronics (spin-polarized current source), quantum optics, and quantum computing.

ACKNOWLEDGMENTS

We acknowledge support from the European Union's Horizon 2020 Research and Innovation Programme under Grant Agreement No. 766714/HiTIME.

Appendix: Hamiltonian on the curved surface

The surface of the TINW can be described using the space time metric in 2+1D (z, ϕ, t)

$$g_{\mu,\nu} = (-1, 1 + R'^2, R^2), \quad (10)$$

where R' is the change in radius along the nanowire. This metric is related to the Minkowski metric for the flat surface by the following relation

$$g_{a,b} = g_{\mu,\nu} e^\mu_a e^\nu_b, \quad (11)$$

Here Latin letters (a, b) denote the local coordinates and Greek letters (μ, ν) denote general coordinates. The Dirac equation in curved space is

$$i\gamma^\mu D_\mu \psi = 0, \quad (12)$$

where the covariant derivative, $D_\mu = \partial_\mu + \omega_{ab\mu} \Sigma^{ab}/4$. It can be shown that only $\omega_{12\phi}$ and $\omega_{21\phi}$ are non zero²³ and given by

$$\omega_{12\phi} = \omega_{21\phi} = \frac{R'}{\sqrt{1 + R'^2}}, \quad (13)$$

so the covariant derivatives are given by

$$\begin{aligned} D_t &= \partial_t, \\ D_z &= \partial_z, \\ D_\phi &= \partial_\phi + \omega_{12\phi} \Sigma^{21}/2. \end{aligned} \quad (14)$$

Using these expressions we can write the Dirac Eq.(12) as

$$i\gamma^t \partial_t \psi + i\gamma^z \partial_z \psi + i\gamma^\phi [\partial_\phi + \omega_{12\phi} \Sigma^{21}/2] \psi = 0, \quad (15)$$

where

$$\Sigma^{21} = \frac{1}{2} [\Gamma^1, \Gamma^2] \quad \text{and} \quad \gamma^\mu \equiv e^\mu_a \Gamma^a. \quad (16)$$

To calculate vierbein or tetrad, $(e^\mu)_a$ we use Eq.(11) and find three set of equations

$$\begin{aligned} g_{00} &= g_{\mu\nu} e^\mu_0 e^\nu_0, \\ g_{11} &= g_{\mu\nu} e^\mu_1 e^\nu_1, \\ g_{22} &= g_{\mu\nu} e^\mu_2 e^\nu_2, \end{aligned} \quad (17)$$

which can be expanded in terms of the components of $g_{\mu\nu}$ as

$$\begin{aligned} -1 &= -(e^t_0)^2 + (1 + R'^2)(e^z_0)^2 + R^2(e^\phi_0)^2, \\ -1 &= -(e^t_1)^2 + (1 + R'^2)(e^z_1)^2 + R^2(e^\phi_1)^2, \\ -1 &= -(e^t_2)^2 + (1 + R'^2)(e^z_2)^2 + R^2(e^\phi_2)^2, \end{aligned} \quad (18)$$

now taking only the following tetrad non-zero

$$\begin{aligned} e^t_0 &= 1, \\ e^z_1 &= \frac{1}{\sqrt{1 + R'^2}}, \\ e^\phi_2 &= \frac{1}{R}, \end{aligned} \quad (19)$$

we find γ^μ using Eq.(16)

$$\begin{aligned} \gamma^t &\equiv e^t_a \Gamma^a = e^t_0 \Gamma^0 + e^t_1 \Gamma^1 + e^t_2 \Gamma^2 = \Gamma^0, \\ \gamma^z &\equiv e^z_a \Gamma^a = e^z_0 \Gamma^0 + e^z_1 \Gamma^1 + e^z_2 \Gamma^2 = \frac{1}{\sqrt{1 + R'^2}} \Gamma^1, \\ \gamma^\phi &\equiv e^\phi_a \Gamma^a = e^\phi_0 \Gamma^0 + e^\phi_1 \Gamma^1 + e^\phi_2 \Gamma^2 = \frac{1}{R} \Gamma^2. \end{aligned} \quad (20)$$

We can put these results in Eq.(15) and get

$$\begin{aligned} i\Gamma^0 \partial_t \psi + i \frac{1}{\sqrt{1 + R'^2}} \Gamma^1 \partial_z \psi + i \frac{1}{R} \Gamma^2 \left[\partial_\phi \right. \\ \left. + \frac{R'}{\sqrt{1 + R'^2}} \Sigma^{21}/2 \right] \psi = 0. \end{aligned} \quad (21)$$

Now, we choose the following Dirac matrices

$$\begin{aligned} \Gamma^0 &= i\sigma_x, \\ \Gamma^1 &= i\sigma_y, \\ \Gamma^2 &= i\sigma_z, \end{aligned} \quad (22)$$

and write Eq. (21) as

$$\begin{aligned} -\sigma_x \partial_t \psi + i \frac{1}{\sqrt{1 + R'^2}} \sigma_z \partial_z \psi + \sigma_y \frac{i}{R} \left[\partial_\phi \right. \\ \left. + \frac{R'}{\sqrt{1 + R'^2}} \Sigma^{21}/2 \right] \psi = 0, \end{aligned} \quad (23)$$

where

$$\Sigma^{21} = \frac{1}{2} [\Gamma^2, \Gamma^1] = i\sigma_x.$$

Inserting \hbar and v_F we arrive at the following Hamiltonian

$$-i\hbar\sigma_x \partial_t \psi = v_F \left[\frac{1}{\sqrt{1 + R'^2}} \sigma_z \left\{ ip_z + \frac{\hbar R'}{2R} \right\} + \frac{\hbar}{R} \sigma_y \partial_\phi \right] \psi. \quad (24)$$

We can simplify by multiplying both sides by $-\sigma_x$ and get the following Hamiltonian

$$H = v_F \left[\frac{1}{\sqrt{1 + R'^2}} \left\{ i\hbar \partial_z + \frac{i\hbar R'}{2R} \right\} \sigma_y - \frac{i\hbar}{R} \sigma_z \partial_\phi \right]. \quad (25)$$

- ¹ H. Peng, K. Lai, D. Kong, S. Meister, Y. Chen, X.-L. Qi, S.-C. Zhang, and Z.-X. Shen & Y. Cui, “Aharonov-Bohm interference in topological insulator nanoribbons,” *Nature Materials* **9**, 225–229 (2010).
- ² L. A. Jauregui, M. T. Pettes, L. P. Rokhinson, and L. Shi & Y. P. Chen, “Magnetic field-induced helical mode and topological transitions in a topological insulator nanoribbon,” *Nature Nanotechnology* **11**, 345–351 (2016).
- ³ S. Y. Matsushita, K. K. Huynh, and K. Tanigaki, “Ultrathin film of 3d topological insulators by vapor-phase epitaxy: Surface dominant transport in wide temperature revealed by Seebeck measurement,” *Nature Nanotechnology* **99**, 195302 (2019).
- ⁴ J. H. Bardarson, P. W. Brouwer, and J. E. Moore, “Aharonov-Bohm oscillations in disordered topological insulator nanowires,” *PRL* **105**, 156803 (2010).
- ⁵ E. J. König, P. M. Ostrovsky, I. V. Protopopov, and A. D. Mirlin, “Interaction and disorder effects in three-dimensional topological insulator thin films,” *PRB* **85**, 195130 (2012).
- ⁶ L. Fu and C. L. Kane, “Topology, delocalization via average symmetry and the symplectic Anderson transition,” *PRL* **109**, 246605 (2012).
- ⁷ P. M. Ostrovsky, I. V. Gornyi, and A. D. Mirlin, “Interaction-induced criticality in Z_2 topological insulators,” *PRL* **105**, 036803 (2010).
- ⁸ S. Ryu, C. Mudry, H. Obuse, and A. Furusaki, “ Z_2 topological term, the global anomaly, and the two-dimensional symplectic symmetry class of Anderson localization,” *PRL* **99**, 116601 (2007).
- ⁹ P. Roushan, J. Seo, C. V. Parker, Y. S. Hor, D. Hsieh, D. Qian, A. Richardella, M. Z. Hasan, R. J. Cava, and A. Yazdani, “Topological surface states protected from backscattering by chiral spin texture,” *Nature* **460**, 11006–1109 (2009).
- ¹⁰ M. Z. Hasan and C. L. Kane, “Colloquium: Topological insulators,” *RMP* **82**, 3045 (2010).
- ¹¹ T. Zhang, Y. Jiang, Z. Song, H. Huang, Y. He, Z. Fang, H. Weng, and Chen Fang, “Catalogue of topological electronic materials,” *Nature* **566**, 475–479 (2019).
- ¹² A. Soumyanarayanan, N. Reyren, A. Fert, and C. Panagopoulos, “Emergent phenomena induced by spin-orbit coupling at surfaces and interfaces,” *Nature* **539**, 509–517 (2016).
- ¹³ Tobias W. Schmitt, Malcolm R. Connolly, Michael Schleenvoigt, Chenlu Liu, Oscar Kennedy, José M. Chávez-García, Abdur R. Jalil, Benjamin Bennemann, Stefan Trelenkamp, Florian Lentz, Elmar Neumann, Tobias Lindström, Sebastian E. de Graaf, Erwin Berenschot, Niels Tas, Gregor Mussler, Karl D. Petersson, Detlev Grützmacher, and Peter Schüffelgen, “Integration of topological insulator Josephson junctions in superconducting qubit circuits,” *Nano Lett.* **22**, 2595–2602 (2022).
- ¹⁴ G. J. Ferreira and D. Loss, “Magnetically defined qubits on 3d topological insulators,” *PRL* **111**, 106802 (2013).
- ¹⁵ L. Fu and C. L. Kane, “Superconducting proximity effect and Majorana fermions at the surface of a topological insulator,” *PRL* **100**, 096407 (2008).
- ¹⁶ Yi Zhang, Ke He, Cui-Zu Chang, Can-Li Song, Li-Li Wang, Xi Chen, Jin-Feng Jia, Zhong Fang, Xi Dai, Wen-Yu Shan, Shun-Qing Shen, Qian Niu, Xiao-Liang Qi, Shou-Cheng Zhang, Xu-Cun Ma, and Qi-Kun Xue, “Crossover of the three-dimensional topological insulator Bi₂Se₃ to the two-dimensional limit,” *Nature Physics* **6**, 584–588 (2010).
- ¹⁷ J. Linder, T. Yokoyama, and A. Sudbo, “Anomalous finite size effects on surface states in the topological insulator Bi₂Se₃,” *PRB* **80**, 205401 (2009).
- ¹⁸ C.-X. Liu, H. Zhang, B. Yan, X.-L. Qi, T. Frauenheim, Z. Fang X. Dai, and S.-C. Zhang, “Oscillatory crossover from two-dimensional to three-dimensional topological insulators,” *PRB* **81**, 041307(R) (2010).
- ¹⁹ H.-Z. Lu, W.-Y. Shan, W. Yao, Q. Niu, and S.-Q. Shen, “Massive Dirac fermions and spin physics in an ultrathin film of topological insulator,” *PRB* **81**, 115407 (2010).
- ²⁰ S. Cho, D. Kim, P. Syers, N. P. Butch, J. Paglione, and M. S. Fuhrer, “Topological insulator quantum dot with tunable barriers,” *Nano Lett.* **12**, 469 (2012).
- ²¹ Raphael Kozlovsky, Ansgar Graf, Denis Kochan, Klaus Richter, and Cosimo Gorini, “Magnetoconductance, quantum Hall effect, and Coulomb blockade in topological insulator nanocones,” *PRL* **124**, 126804 (2020).
- ²² E. Xypakis, J.-W. Rhim, J. H. Bardarson, and R. Ilan, “Perfect transmission and Aharonov-Bohm oscillations in topological insulator nanowires with nonuniform cross section,” *PRB* **101**, 045401 (2020).
- ²³ F. d. Juan, J. H. Bardarson, and R. Ilan, “Conditions for fully gapped topological superconductivity in topological insulator nanowires,” *SciPost Physics* **6** (2019), 10.21468/SciPostPhys.6.5.060.
- ²⁴ Y. Takane and K.-I. Imura, “Unified description of Dirac electrons on a curved surface of topological insulators,” *Journal of the Physical Society of Japan* **82**, 074712 (2013).
- ²⁵ F. Munning, O. Breunig, H. F. Legg, S. Roitsch, D. Fan, M. Robler, and A. Rosch & Y. Ando, “Quantum confinement of the Dirac surface states in topological-insulator nanowires,” *Nature Communications* **12**, 1038 (2021).
- ²⁶ R. Tsu and L. Esaki, “Tunneling in a finite superlattice,” *App. Phys. Lett.* **22**, 562 (1973).
- ²⁷ Yi Zhang and Ashvin Vishwanath, “Anomalous Aharonov-Bohm conductance oscillations from topological insulator surface states,” *PRL* **105**, 206601 (2010).
- ²⁸ C. Koke, C. Noh, and D. G. Angelakis, “Dirac equation in 2-dimensional curved spacetime, particle creation, and coupled waveguide arrays,” *Annals of Physics* **374**, 162–178 (2016).
- ²⁹ V. Parente, P. Lucignano, P. Vitale, A. Tagliacozzo, and F. Guinea, “Spin connection and boundary states in a topological insulator,” *PRB* **83**, 075424 (2011).
- ³⁰ R. Egger, A. Zazunov, and A. Levy Yeyati, “Helical Luttinger liquid in topological insulator nanowires,” *PRL* **105**, 136403 (2010).
- ³¹ A. Kundu, A. Zazunov, A. Levy Yeyati, T. Martin, and R. Egger, “Energy spectrum and broken spin-surface locking in topological insulator quantum dots,” *PRB* **83**, 125429 (2011).
- ³² S. S. Hong, Y. Zhang, J. J. Cha, X.-L. Qi, and Y. Cui, “One-dimensional helical transport in topological insulator nanowire interferometers,” *Nano Lett.* **14**, 2815–2821 (2014).
- ³³ V. V. Cheianov and V. I. Falko, “Selective transmission of Dirac electrons and ballistic magnetoresistance of $n-p$ junctions in graphene,” *PRB* **74**, 041403(R) (2006).

- ³⁴ K.-K. Bai, J.-B. Qiao¹, H. Jiang, H. Liu, and L. He, “Massless Dirac fermions trapping in a quasi-one-dimensional npn junction of a continuous graphene monolayer,” *PRB* **95**, 201406 (2017).
- ³⁵ S. Modak, K. Sengupta, and Diptiman Sen, “Spin injection into a metal from a topological insulator,” *PRB* **86**, 205114 (2012).
- ³⁶ Oindrila Deb, Abhiram Soori, and Diptiman Sen, “Edge states of a three-dimensional topological insulator,” *J. Phys.: Condens. Matter* **26**, 315009 (2014).
- ³⁷ C. Gutierrez, L. Brown, C.-J. Kim, J. Park, and A. N. Pasupathy, “Klein tunnelling and electron trapping in nanometre-scale graphene quantum dots,” *Nat. Phys.* **12**, 1069 (2016).
- ³⁸ J.-B. Qiao, H. Jiang, H. Liu, H. Yang, N. Yang, K.-Y. Qiao, and L. He, “Bound states in nanoscale graphene quantum dots in a continuous graphene sheet,” *PRB* **95**, 081409 (2017).
- ³⁹ M.-H. Liu, C. Gorini, and K. Richter, “Creating and steering highly directional electron beams in graphene,” *PRL* **118**, 066801 (2017).
- ⁴⁰ A. F. Young and P. Kim, “Quantum interference and Klein tunnelling in graphene heterojunctions,” *Nat. Phys.* **5**, 222–226 (2009).
- ⁴¹ S. Cho, B. Dellabetta, J. Schneeloch R. Zhong, T. Liu, G. Gu, M. J. Gilbert, and N. Mason, “Aharonov–Bohm oscillations in a quasi-ballistic three-dimensional topological insulator nanowire,” *Nature Communications* **6**, 7634 (2015).
- ⁴² Yi Zhang, Ying Ran, and Ashvin Vishwanath, “Topological insulators in three dimensions from spontaneous symmetry breaking,” *PRB* **79**, 245331 (2009).
- ⁴³ Jens Hjorleifur Bardarson and Roni Ilan, “Transport in topological insulator nanowires,” *arXiv: Mesoscale and Nanoscale Physics*, 93–114 (2018).
- ⁴⁴ Supriyo Datta, *Electronic Transport in Mesoscopic Systems*, Cambridge Studies in Semiconductor Physics and Microelectronic Engineering (Cambridge University Press, 1995).
- ⁴⁵ C. W. J. Beenakker, “Theory of Coulomb-blockade oscillations in the conductance of a quantum dot,” *PRL* **44**, 1646 (1991).
- ⁴⁶ P. L. McEuen, E. B. Foxman, U. Meirav, M. A. Kastner, Y. Meir, N. S. Wingreen, and S. J. Wind, “Transport spectroscopy of a Coulomb island in the quantum Hall regime,” *PRL* **66**, 1928 (1991).
- ⁴⁷ I.L. Aleiner, P.W. Brouwer, and L.I. Glazman, “Quantum effects in Coulomb blockade,” *Physics Reports* **358**, 309–440 (2002).